Urban Rail Transit
https://doi.org/10.1007/s40864-025-00261-9
http://www.urt.cn/

ORIGINAL RESEARCH PAPERS

Rail Profile Matching Assessment and Selection for Sharp Radius Curves in Urban Metro: A Case Study

Bolun An[1,2] · Wei Lu[1,3,4] · Fengshou Liu[1,2] · Hao Liu[1,3,4] · Yang Xu[1,3,4] · Sen Wang[1,3,4]

Received: 4 September 2025 / Revised: 20 October 2025 / Accepted: 2 November 2025

Abstract Urban rail transit systems contain numerous sharp radius curves where rail fatigue defect occurs frequently. In severe cases, this leads to extensive rail scaling, rail surface fatigue cracks, and intensified wheel-rail vibration and noise. Appropriate rail profiles can effectively optimise wheel-rail contact status and mitigate the deterioration development of wear and wheel/rail fatigue defect. Addressing this issue, this paper combines field testing evaluation and simulation analysis methods to establish a metro vehicle-track coupled dynamics model validated by measured data. Three profile schemes and three simulation scenarios were considered to comprehensively study and analyze the matching performance between sharp radius curve rail profiles and actual wheel profiles from perspectives of wheel-rail contact stress distribution, fatigue and wear indices, and vehicle dynamic performance.

Results indicate that the 60N profile consistently exhibits its optimal stress control effectiveness under all operating conditions. Compared to the traditional 60 profile condition, normal and tangential contact stress are reduced by up to 64% and 61%, respectively. Relative to the measured profile condition, stress reductions of up to 64% and 45% are achieved at the gauge corner. The 60N profile demonstrates the lowest fatigue index compared to the 60 profile and measured profile, while maintaining stable wear characteristics and improving vehicle lateral stability with reduced bogie acceleration peaks. Based on comprehensive analysis, the 60N profile is recommended as the optimal solution for both original rail profile selection and grinding target profile.

Keywords Urban metro · Wheel-rail fatigue defect · Rail profile · Wheel-rail contact stress

1 Introduction

Urban rail transit systems have become essential infrastructure for metropolitan transportation, with metro systems serving as the primary mode of daily commute for millions of passengers worldwide. Due to spatial constraints in underground construction and the necessity to navigate around existing structures and geological features, metro lines inevitably incorporate numerous sharp radius curves, particularly in densely developed urban areas.

These sharp curves present significant challenges to vehicle-track interaction dynamics. When trains negotiate sharp radius curves, the wheel-rail contact conditions become considerably more complex compared to tangent tracks. The contact stress distribution experiences dramatic variations, leading to accelerated rail degradation including side wear, rolling contact fatigue, corrugation, and other defects [1–5]. Without timely intervention, these defects progressively deteriorate rail performance, reduce service life, and potentially develop into critical failures such as rail breaks, posing serious safety risks to system operation.

Rail grinding remains one of the most effective maintenance strategies [6–8]: it both removes surface defects and

✉ Fengshou Liu
harve78@163.com

✉ Hao Liu
864845592@qq.com

1 China Academy of Railway Sciences Corporation Limited, Beijing, China

2 Metals and Chemistry Research Institute, China Academy of Railway Sciences Corporation Limited, Beijing, China

3 State Key Laboratory of High-Speed Railway Track System, Beijing 10008l, China

4 Railway Engineering Research Institute, China Academy of Railway Sciences Corporation Limited, Beijing, China

reshapes the rail profile to improve ride quality and optimize wheel–rail contact status. Its effectiveness, however, hinges on an accurate understanding of defect mechanisms and the judicious selection of the target profile. It is therefore essential to quantify how profile selection affects wheel–rail contact in sharp curves and to identify the most appropriate grinding target—work that underpins science-based maintenance strategies and extends the service life of metro rails.

A growing amount of work has carried on wheel–rail profile matching and profile optimization for sharp-radius curves in urban metros. In terms of wheel-rail profile matching, Zhang et al. analyzed the influence of different wheel-rail profile matching on the operational quality of metro vehicles, concluding that rational control of the equivalent conicity in wheel-rail profile matching is critical for improving vehicle operational performance [9]. Zhou et al. found through simulation analysis that new rail profiles are prone to wheel-rail contact stress concentration and rapid wear. As rail gauge wear increases, the wheel-rail contact state transitions to two-point contact, with high contact stress likely to occur at the gauge corner, accelerating wear and fatigue defect initiation [10]. Tao et al. investigated the matching performance of LM, S1002, and DIN5573 wheel profiles with the 60 rail profile under different rail cant conditions, demonstrating that the commonly used LM profile is insensitive to rail cant and exhibits best curve negotiation performance at the rail cant of 1/40 [11]. Chen et al. studied the matching performance of LM wheel profile with the 60 profile at different track gauges, showing that appropriate gauge widening can reduce wear and fatigue defect [12].

Regarding rail profile optimization, Yang et al. proposed asymmetric grinding profiles using multi-objective optimization algorithms, which effectively reduce rail wear [13]. Wang et al. proposed measures to extend the service life of high rail profiles by repairing low rail profiles and implementing wayside lubrication in metro curve sections [1]. Qi et al. developed optimized profiles for metro sharp radius curves based on the KSM-PSO optimization algorithm, with simulation results showing that these profiles can effectively reduce the wear rate of high rails in curves [6]. Cui et al. proposed a rail grinding profile design scheme and conducted field applications, reducing wheel-rail wear and improving vehicle operational performance [14].

Whether through wheel-rail profile assessment or profile optimization, the objective is to provide reference for rail grinding target profiles to reduce excessive wear and rail surface fatigue defects in sharp-radius curve sections, thereby extending rail service life. Urban rail transit systems have complex operating conditions and alignments, with varying problems and requirements across different sections. Therefore, rail profile selection or optimization must be based on field requirements to develop highly applicable and targeted selection schemes. However, existing research on metro rail profile selection and optimization has limited integration of actual service conditions for both wheel and rail parts. Many proposed optimization schemes are designed primarily for grinding applications and face practical challenges when used as original profiles for new rails or major rail replacement projects.

Currently, China's high-speed railway and general speed railway have fully adopted the 60N profile as the target profile for rail grinding. This profile features a lower gauge corner compared to the conventional 60 profile, reducing contact stress at the gauge corner [15–17] and decreasing the development of wear and fatigue defect. Some urban rail transit systems still use aging rail equipment with 60 rail profiles, and the short maintenance windows make timely grinding and repair difficult [18]. Therefore, determining reasonable and effective original rail profiles and grinding target profiles is crucial for improving rail grinding efficiency, rail major replacement efficiency, and service performance and life.

Based on this background, this paper takes Metro Line 2 in City N as the research case study. Starting from field investigation and testing, a metro vehicle-track coupled dynamics model is established to evaluate and compare the matching performance of the 60 rail profile, 60N rail profile, and measured profiles with measured wheel profiles from the perspectives of wheel-rail contact status, stress, and vehicle dynamic performance. The optimal profile scheme is identified to provide theoretical support for rail selection and grinding target profile determination.

The structure of this paper is organized as follows: Sec. 2 presents field investigation and testing of rail service conditions, including rail surface defect states, rail profile conditions, and track alignment parameters. Sec. 3 establishes and validates the simulation model, using measured wheel profiles and in-service vehicle parameters to develop a metro vehicle-track coupled dynamics model, with model reliability validated through track inspection vehicle test data and field wayside dynamics test data. Sec. 4 analyzes and evaluates rail profile service performance, considering three simulation scenarios to identify the optimal profile from the perspectives of wheel-rail contact status, stress, and vehicle dynamic performance. Sec. 5 provides conclusions and prospects, summarizing the main research achievements and proposing directions for future research.

2 Investigation of Rail Service Status

An investigation of the rail service conditions on Metro Line 2 in City N was conducted, primarily covering rail surface conditions, rail profiles, rail irregularity, and simulation conditions were established based on actual track alignment parameters in the sharp radius curve sections.

2.1 Status of Rail Surface

The working side of the high rail in curve sections shows nearly full contact band with severe side wear. Field observation reveals that the brightest region within the contact band is located at the gauge corner, where dense contact fatigue cracks and continuous scaling are present, significantly affecting rail surface smoothness. Rail surface irregularity testing equipment was used to measure the irregularity at scaling locations. Fig. 1b shows the measured rail surface irregularity at three selected measurement points and a normal section (without scaling). It can be observed that the maximum irregularity amplitude at all three measurement points exceeds 0.2 mm, with some locations reaching depths above 0.4 mm which intensifies wheel-rail vibration, affects the service life of wheel-rail components, and also causes crack initiation, reducing rail service life.

2.2 Status of Rail Profile

Due to the need to analyze rail profile conditions, rail profiles in curve sections of this line were tested. Rail side wear was found on the high rail, with some measured profiles showing side wear exceeding 12 mm. When analyzing profile conditions, the profiles were aligned with the standard 60 profile (their initial profile) using the method shown in the upper right of Fig. 2, with calculations performed according to the normal angle. The specific alignment method is shown in [15].

Statistical results of all profile deviations for the high rail are presented in Fig. 2. It can be observed that almost

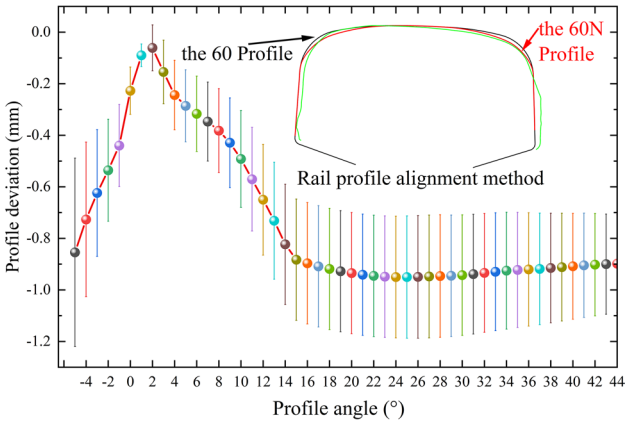

Fig. 2 Deviation of measured rail profiles

all profiles exhibit negative deviations, with the average profile deviation reaching nearly 1 mm beyond 15°. This indicates that the actual rail gauge corner curvature in the field is larger than initial profile, which concentrates wheel-rail contact area more toward the rail running surface center. Beyond 15°, the mean deviation reaches 1 mm, with a maximum value approaching − 1.2 mm and a minimum value of − 0.6 mm. This indicates that the actual rail gauge curvature is small, which tends to cause wheel-rail two-point contact, with the wheel-rail contact point on the running surface positioned closer to the center, and the contact point at the gauge corner positioned closer to the rail fillet. The high dispersion indicates that sections

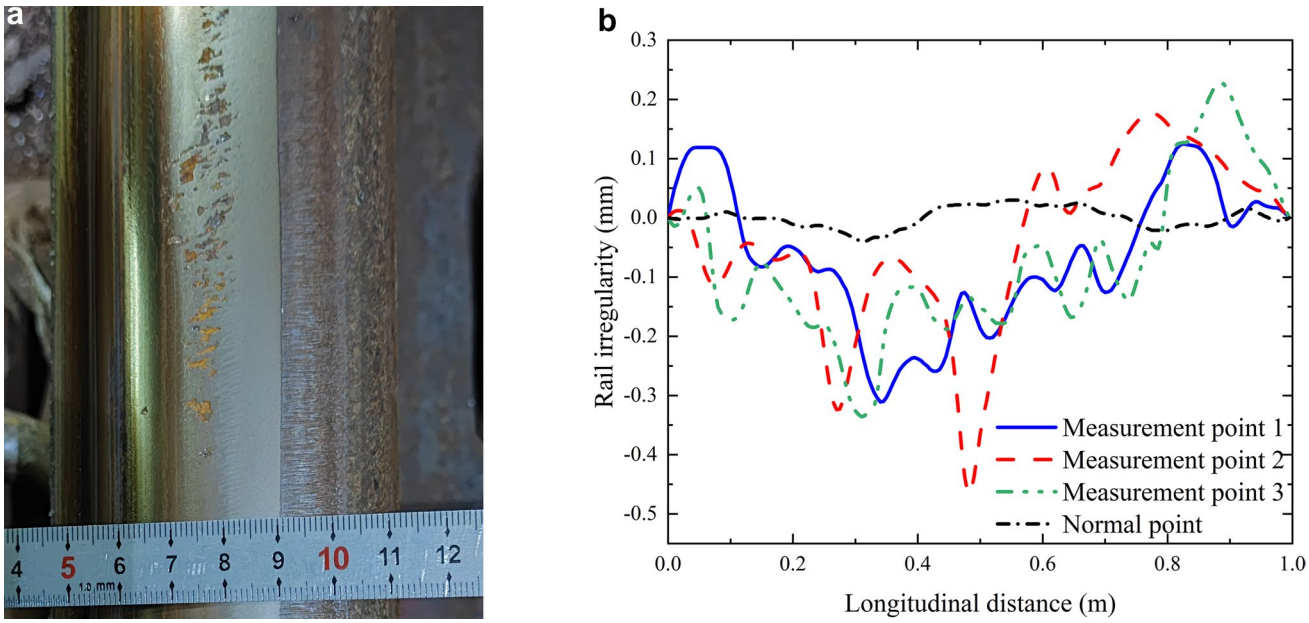

Fig. 1 Rail scaling and the irregularity

with large negative deviations will experience wheel-rail stress concentration.

2.3 Track Alignment Parameter

The field curve begins at K15+197, with a transition curve length of 60 m, curve radius of 320 m, and actual superelevation of 120 mm. In the simulation model, the straight section length was set to 197 m and the circular curve section to 550 m, as shown in Fig. 3. Additionally, field test results indicate that vehicles pass through this curve section at approximately 40 km/h, with about 60 mm excess superelevation, which is unfavorable for curve negotiation and increases wheel-rail tangential stress, promoting more rapid initiation of contact fatigue defect.

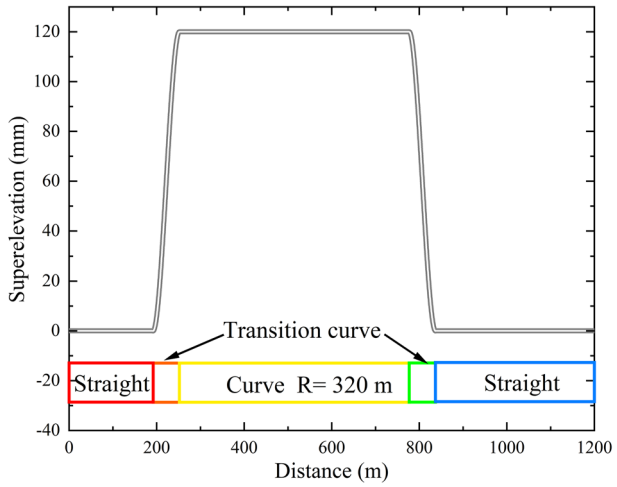

Fig. 3 Alignment parameters of the sharp radius curve

3 Simulation Model Establishment and Validation

This section introduces the simulation analysis model established based on the metro operating vehicles, as well as the wheel profiles adopted. The model accuracy was validated based on test results.

3.1 Simulation Model Establishment

The vehicles used in this city are Metro Type B vehicles. Based on vehicle parameters [19], this paper employs multi-body dynamics methods to establish a metro vehicle-track coupled dynamics model. The model includes car body, bogie, wheelset, and track. Vehicle structural components are connected through primary and secondary suspensions as shown in Fig. 4. Non-Hertzian contact [20, 21] is adopted to calculate the wheel-rail contact states and stresses.

The algorithm is based on the strip-division method implemented in our multi-body dynamics simulation platform. The core calculation procedure is as follows. The contact patch is divided into strips along the longitudinal direction. To obtain the correct contact ellipse shape, the relative curvature A in the rolling direction is corrected:

$$\frac{A_c}{A} = \frac{1}{\lambda}\left(\frac{n}{m}\right)^2 \tag{1}$$

where $\lambda = a/b$ is the curvature ratio, and m, n are Hertzian parameters calculated for each strip.

$$k_i^2 = \left(\frac{a_i}{a}\right)^2 = \frac{h_i}{h_0} \tag{2}$$

where a_i is the half-length of the i-th strip, h_i is the local penetration depth, and h_0 is the penetration at the reference

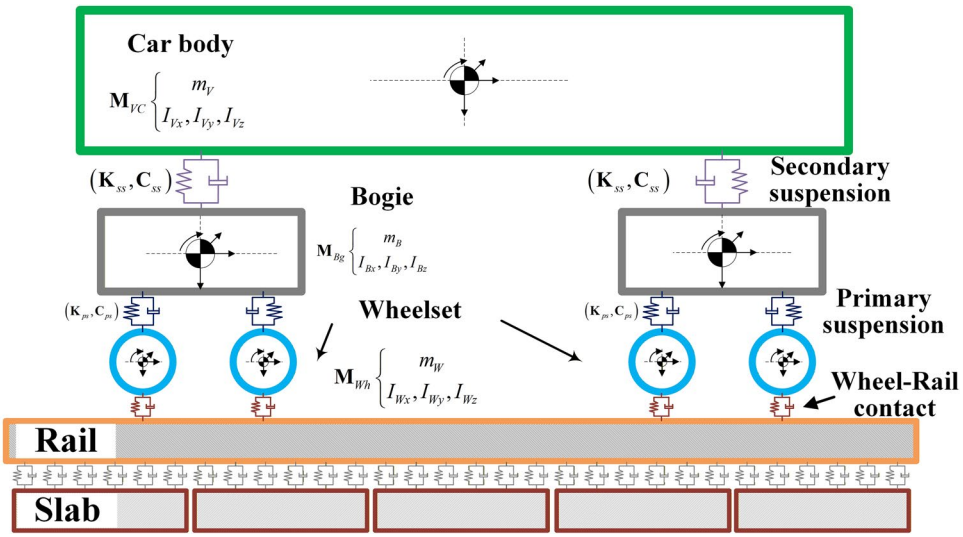

Fig. 4 Metro vehicle-track dynamic model

strip. The normal contact stress on each strip follows the elliptical distribution:

$$\mu\sigma_z = \frac{4}{3\pi}\mu\frac{1+\lambda}{n^3}\frac{E}{1-\nu^2}\frac{h_i}{a_i}\left[1-\left(\frac{x_i}{a_i}\right)^2\right]k_i \tag{3}$$

where E is the elastic modulus, ν is Poisson's ratio, and μ is the friction coefficient. The longitudinal tangential stress is calculated as:

$$\sigma_{xi} = \left(\frac{3}{8}\right)Gc_{11}\nu_{xi}\left(1-\frac{x}{a_i}\right)k_i \tag{4}$$

where G is the shear modulus, c_{11} is the longitudinal creep coefficient, and ν_{xi} is the local longitudinal creepage.

The measured wheel profiles adopted are shown in Fig. 5. The approach involves fitting the profiles of specific wheel positions for each car in a train (for example, fitting the first axle left wheel profile of each vehicle to obtain the first axle left wheel profile in the simulation model). The overall equations of the model are shown as:

$$M_V\ddot{u} + D_V\dot{u} + K_V u = F \tag{5}$$

The mass matrix of the model can be expressed as:

$$M_V = \begin{pmatrix} M_{Vc} & 0 & 0 \\ 0 & M_{Bg} & 0 \\ 0 & 0 & M_{Wh} \end{pmatrix} \tag{6}$$

The damping and stiffness matrices of the model can be expressed as:

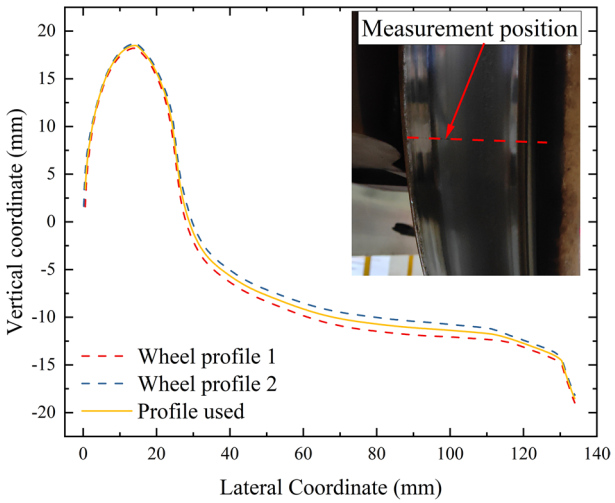

Fig. 5 Measured wheel profile

$$D_V = \begin{pmatrix} D_{CC} & D_{ss} & 0 \\ D_{ss} & D_{BB} & D_{ps} \\ 0 & D_{ps} & D_{WW} \end{pmatrix},\ K_V = \begin{pmatrix} K_{CC} & K_{ss} & 0 \\ K_{ss} & K_{BB} & K_{ps} \\ 0 & K_{ps} & K_{WW} \end{pmatrix} \tag{7}$$

where the subscripts C, B and W represent the car body, the bogie and the wheelset, respectively. *ss* and *ps* represent the secondary suspension and the primary suspension.

The main mass and suspension parameters used in the vehicle model are shown in Table 1.

3.2 Validation of Simulation Model

The model was validated from two aspects. First, validation was conducted based on detection data from the metro track inspection vehicle. By inputting measured metro track irregularities, the car body acceleration obtained through simulation calculation was compared with the acceleration from the inspection vehicle, with results shown in Fig. 6.

According to Fig. 6, the simulation calculation results are close to the inspection vehicle results in terms of both the numerical range and waveform of car body acceleration, with numerical ranges all within − 0.2 to +0.2 m/s^2. A comparison of frequencies corresponding to three peaks in the amplitude-frequency curves of both is shown in Table 2. The frequency deviations for the first peak, second peak, and main peak are all 0.2%, indicating that the vehicle model construction is accurate and reliable.

The wheel-rail forces were measured using the full-bridge shear stress method when the train passed through the ground measurement points. Strain gauges were adhesively bonded to the upper surface of the rail foot at symmetrical cross-sections on both sides of the centerline between two adjacent fasteners, positioned 20 mm from the edge of the rail foot. The spacing between strain gauges was set at 160–240 mm, with the strain gauge orientation at a 45° angle to the longitudinal direction of the rail. After calibrating the strain measurements using a wheel-rail force calibration frame, the lateral wheel-rail forces were calculated.

Table 1 Vehicle model parameters

Item	Value
Mass of the vehicle	33.9 t
Mass of the bogie	3.73 t
Mass of the wheelset	1.73 t
Longitudinal stiffness of the primary suspension	17.2 MN/m
Lateral stiffness of the primary suspension	9.2 MN/m
Vertical stiffness of the primary suspension	347 kN/m
Longitudinal stiffness of the secondary suspension	162 kN/m
Lateral stiffness of the secondary suspension	162 kN/m
Vertical stiffness of the secondary suspension	349 kN/m

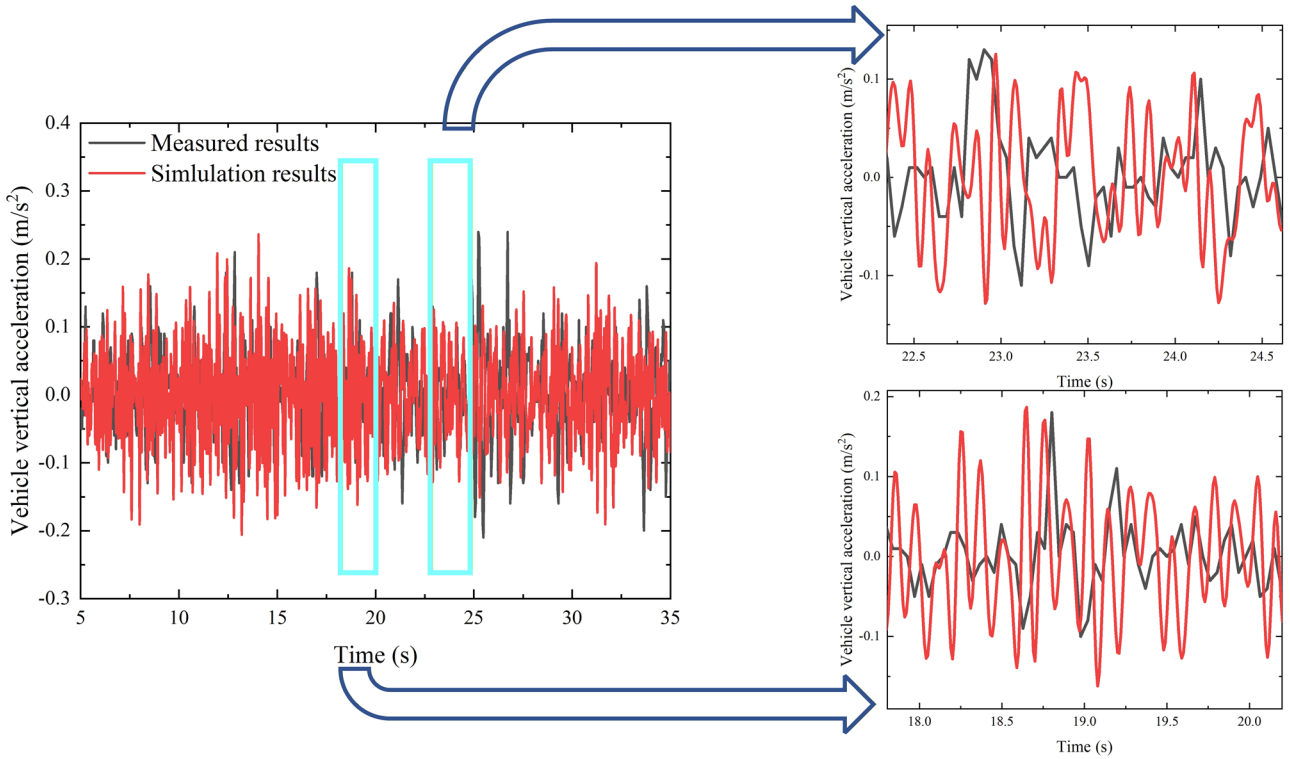

Fig. 6 Comparison of simulation vehicle acceleration with test results

Table 2 Validation in frequency domain

Parameter	Frequency (Hz)		Deviation rate (%)
	Measured	Simulation	
The first peak	0.513	0.514	0.2
The second peak	0.570	0.571	0.2
The highest peak	1.911	1.914	0.2

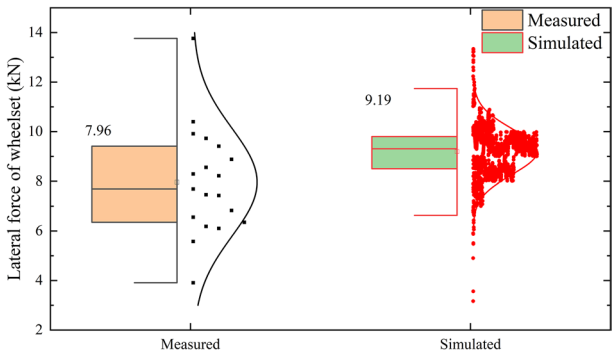

Fig. 7 Comparison of measured wheelset lateral force with simulation results

The comparison of wheelset lateral forces in curve sections is shown in Fig. 7. The simulation calculation result has a mean value of 9.19 kN, slightly higher than the measured result of 7.96 kN, with a difference of approximately 15%. This is because wheelset lateral force is the lateral component of wheel-rail contact normal force, directly affected by axle load, and the vehicle axle load used in simulation calculations may be greater than that of actual operating vehicles. The wayside measurement data collected represents wheel-rail forces from all vehicles passing throughout the day. During working hours, vehicle loads are lighter with correspondingly smaller wheel-rail forces, while during busy times, loads are heavier with larger wheel-rail forces. In the simulation model, the vehicle mass was set to maximum load capacity; therefore, the mean value of measured wheel-rail forces is necessarily lower than the simulation calculation mean value.

The calculated derailment coefficients for left and right wheels in curve sections were compared with measured results, as shown in Fig. 8. It can be observed that the distribution of derailment coefficients obtained from simulation calculations is close to measured results. The mean values for the high rail are 0.32 and 0.33 respectively, with a 3% difference, while the mean derailment coefficients for the low rail are 0.31 and 0.33 respectively, with a 6% difference. Since the derailment coefficient is the ratio of lateral force

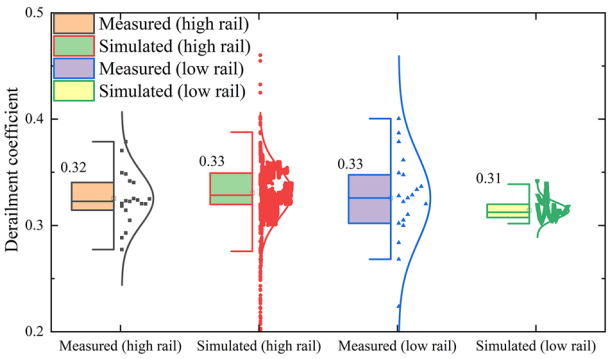

Fig. 8 Comparison of measured derailment coefficient with simulation results

to vertical force, the close agreement between simulation calculation results and measured results also indicates that the proportion of wheel-rail lateral force to vertical force in simulation calculations is close to measured results, validating the reliability of model calculation results.

4 Rail Profile Service Performance Analysis and Evaluation

This section compares and analyzes the service performance of three rail profiles based on the track alignment conditions established in Sec. 2.3: (1) 60 profile; (2) 60N profile; (3) measured profile. To comprehensively evaluate profile performance, three simulation scenarios were established: (1) vehicle passing through ideal curve sections (without track excitation); (2) vehicle passing through sections with irregularities caused by rail surface scaling; (3) vehicle passing through sections with measured track irregularities.

The analysis indicators in this section mainly include wheel-rail contact stress and vehicle dynamic performance. Among them, wheel-rail contact stress is an important indicator reflecting wheel-rail matching in curve sections. High wheel-rail normal contact stress causes plastic deformation on the rail surface that continuously accumulates to form the plastic deformation layer. Under the high wheel-rail tangential contact stress, the plastic deformation layer undergoes shear failure, forming cracks. Therefore, wheel-rail contact stress is the main factor affecting rolling contact fatigue. Vehicle dynamic performance directly relates to train stability and passenger comfort.

4.1 Ideal Condition

Since both the 60N profile and measured profile exhibit two-point contact conditions, the comparative analysis considers both running surface contact and gauge corner contact states separately. The normal contact stress shown in Fig. 9a represents the ratio of wheel-rail normal force to contact patch area, reflecting the overall level of contact stress.

Analysis results indicate that when the vehicle passes through transition curve sections, normal contact stress exhibits significant peaks. The 60 profile condition shows the largest stress peak, approaching 2500 MPa, while the peaks for both 60N profile condition and measured profile condition are similar, around 1490 MPa. Within curve sections, the normal contact stress for the 60 profile is 1411 MPa. The measured profile condition shows uneven contact stress distribution due to continuous profile variations, averaging around 1100 MPa. The 60 N profile condition contact stress is 942 MPa, representing a 33% reduction compared to the 60 rail profile condition and a 14% reduction compared to the measured profile condition.

Wheel-rail contact patch and stress distribution comparison shows: under the 60 rail profile condition, the contact patch is located approximately 30 mm from the running surface center, with maximum contact stress reaching 2050 MPa, where long-term high stress conditions easily cause plastic deformation and fatigue crack initiation. Under 60 N profile condition, the maximum stress on running surface is 1460 MPa and the maximum gauge corner contact stress is 2360 MPa. Under measured profile condition, the maximum stress on running surface is 1540 MPa and the maximum gauge corner contact stress reaches 3280 MPa. For gauge corner contact, the 60N profile shows an average contact stress of approximately 1775 MPa, while the measured profile reaches 2190 MPa. Adopting the 60N profile can reduce gauge corner contact stress by 19%.

Tangential contact stress comparative analysis (Fig. 10) shows that when vehicles pass through transition curve sections, tangential stress reaches peak values: 948 MPa for the 60 rail profile, 648 MPa for the measured profile, and 550 MPa for the 60N profile. After entering curve sections, the distribution pattern remains: the 60 profile condition shows the highest tangential stress (508 MPa), followed by the measured profile (440 MPa), and the 60 N profile shows the lowest (360 MPa). Compared to the 60 profile and measured profile condition, the 60N profile condition reduces wheel-rail tangential stress by 29% and 18%, respectively. Maximum tangential stress within contact patches shows: 962 MPa for the 60 profile, 721 MPa for the measured profile, and 692 MPa for the 60 N profile, representing reductions of 28% and 4% compared to the 60 profile and measured profile, respectively.

At the gauge corner, the measured profile condition shows wheel-rail tangential stress of approximately 810 MPa, while the 60N profile condition shows 670 MPa, a reduction of 17%. The maximum tangential stress under measured profile conditions is 1552 MPa, while the 60N profile shows 1097 MPa, a reduction of 29%.

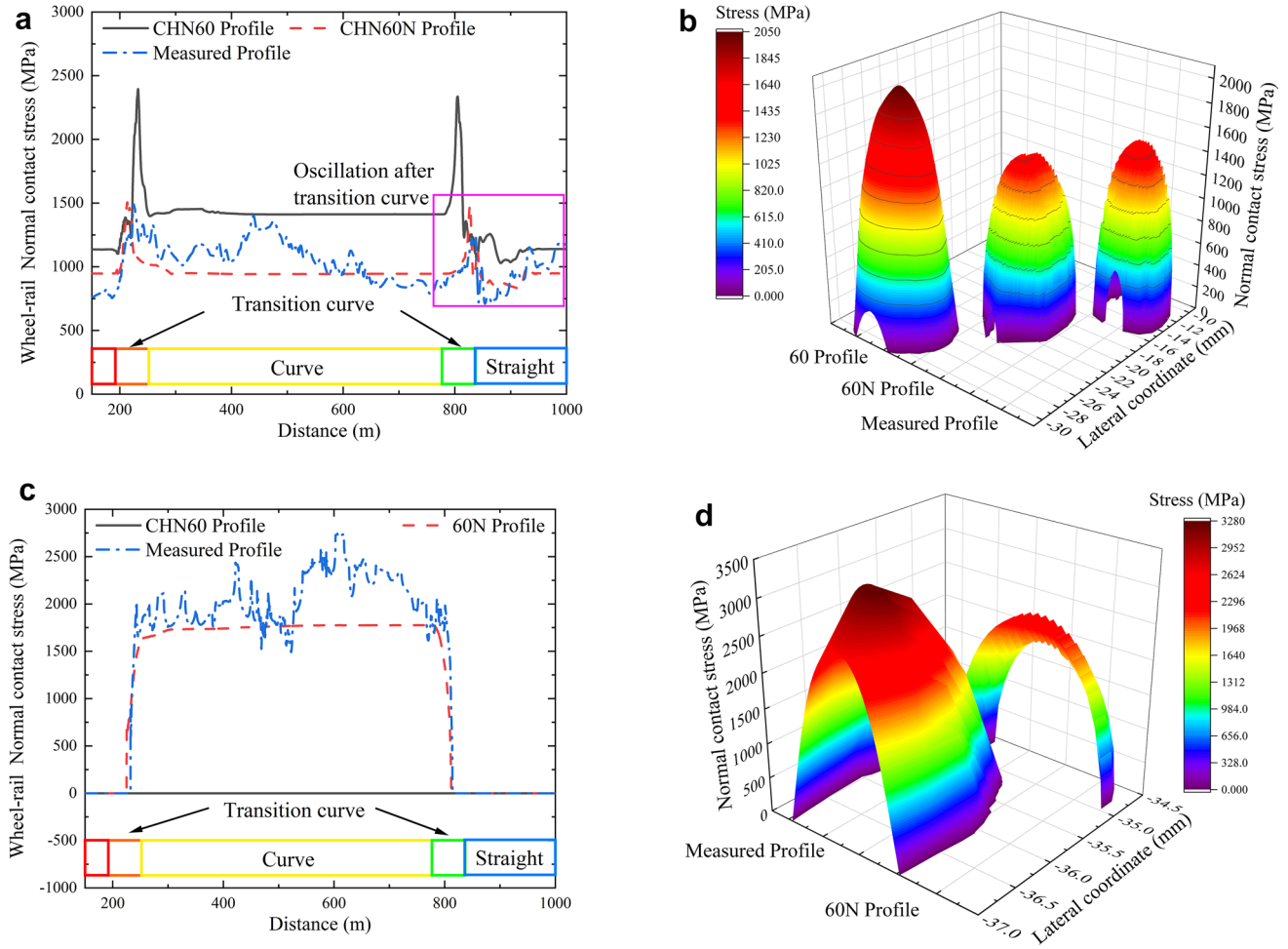

Fig. 9 Comparison of Normal contact stress

Analysis of tangential stress distribution and direction characteristics (shown in Fig. 11) within contact patches reveals: under the 60 profile condition, high tangential stress points are mainly concentrated at 27~28 mm from the running surface center, forming a 13° angle with the lateral direction. Under the 60N profile condition, high tangential stress points are more dispersed, distributed over a range of 17~21 mm, with angles varying from − 2° to 8°. Under measured profile condition, high tangential stress points range from 12~14 mm, with angles mainly at 10°, essentially perpendicular to the fatigue checking direction.

This comparative result indicates that when using the 60N profile, with its wider contact area, lower tangential stress, and more dispersed stress directions, it is less likely to produce concentrated stress within small areas, thus more effectively mitigating fatigue checking initiation.

4.2 Including Rail Irregularity Condition

When rail surface irregularity is considered, wheel-rail forces and contact stress will inevitably increase significantly. This section mainly analyzes the differences in wheel-rail contact stress under different profile conditions. Therefore, one measured irregularity can be used as excitation input for model calculation. The rail irregularities are shown in Fig. 12, with a maximum amplitude of − 0.27 mm. When wheels pass through the defect, wheel-rail contact states change rapidly, resulting in significant peaks in normal and tangential stresses.

When wheels pass through scaling defects, significant differences exist in normal contact stress peak among the three profiles. The maximum stress within the contact patch for the 60 profile reaches 4480 MPa, far exceeding the other two profiles. In comparison, the 60N profile and measured profile show considerably lower stress values of 1600 MPa

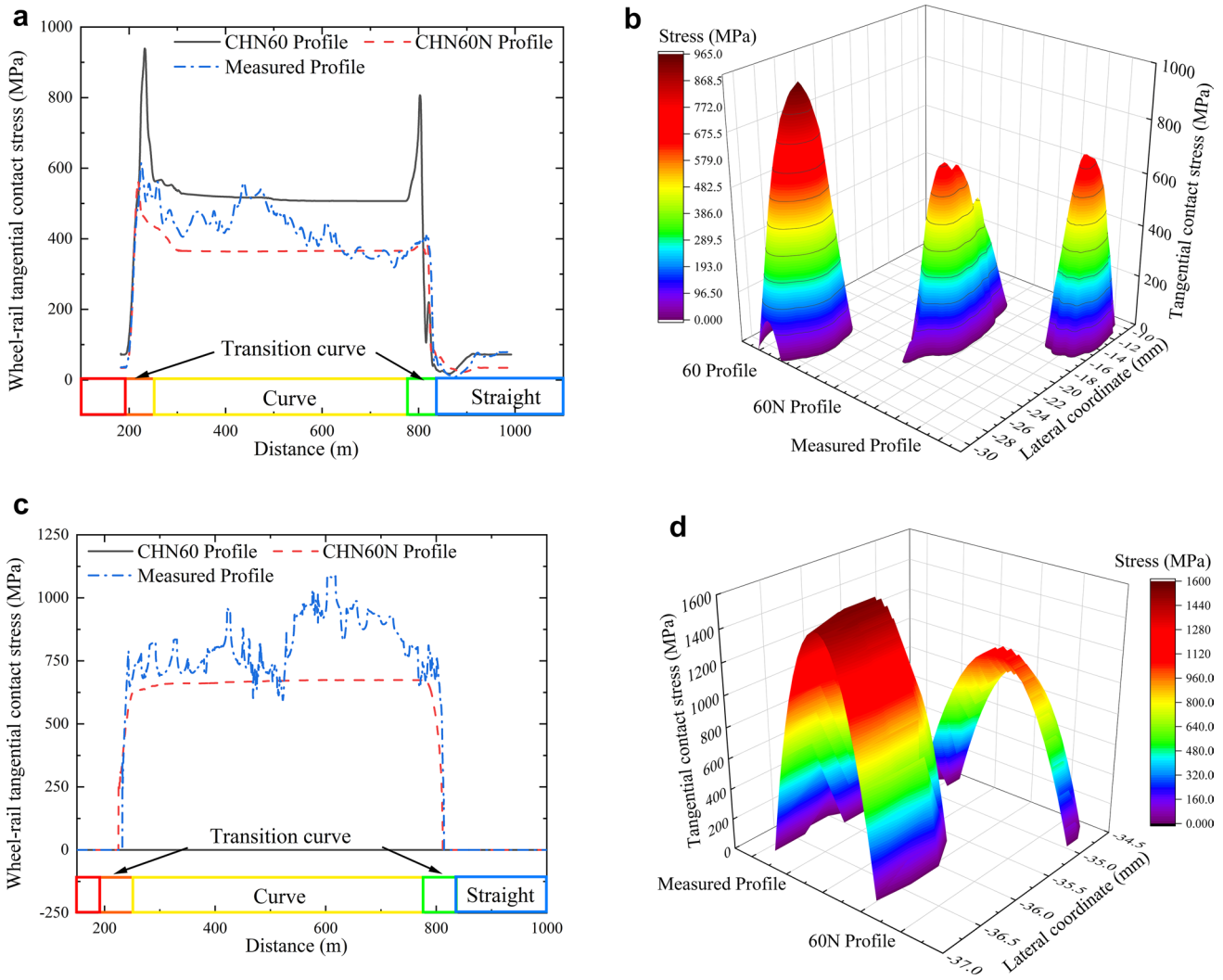

Fig. 10 Comparison of wheel-rail contact tangential stress

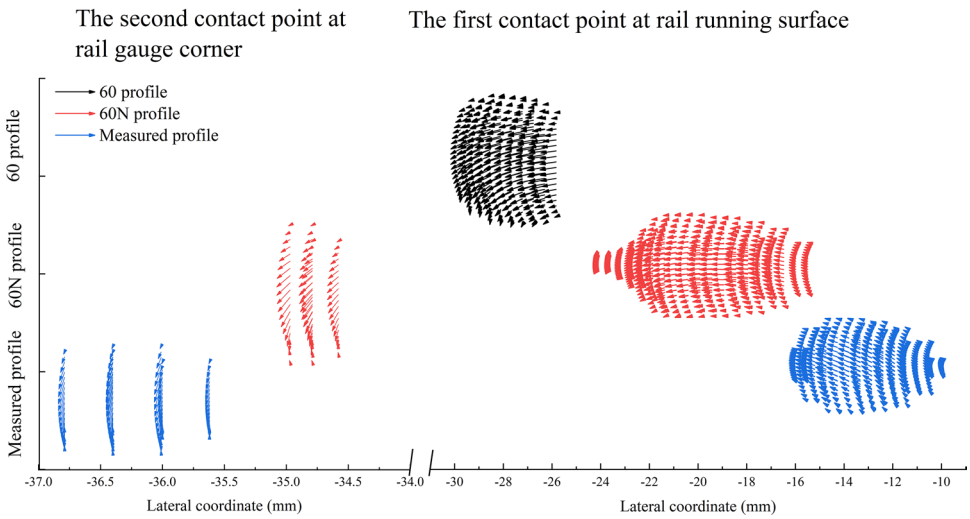

Fig. 11 Direction of the tangential stress

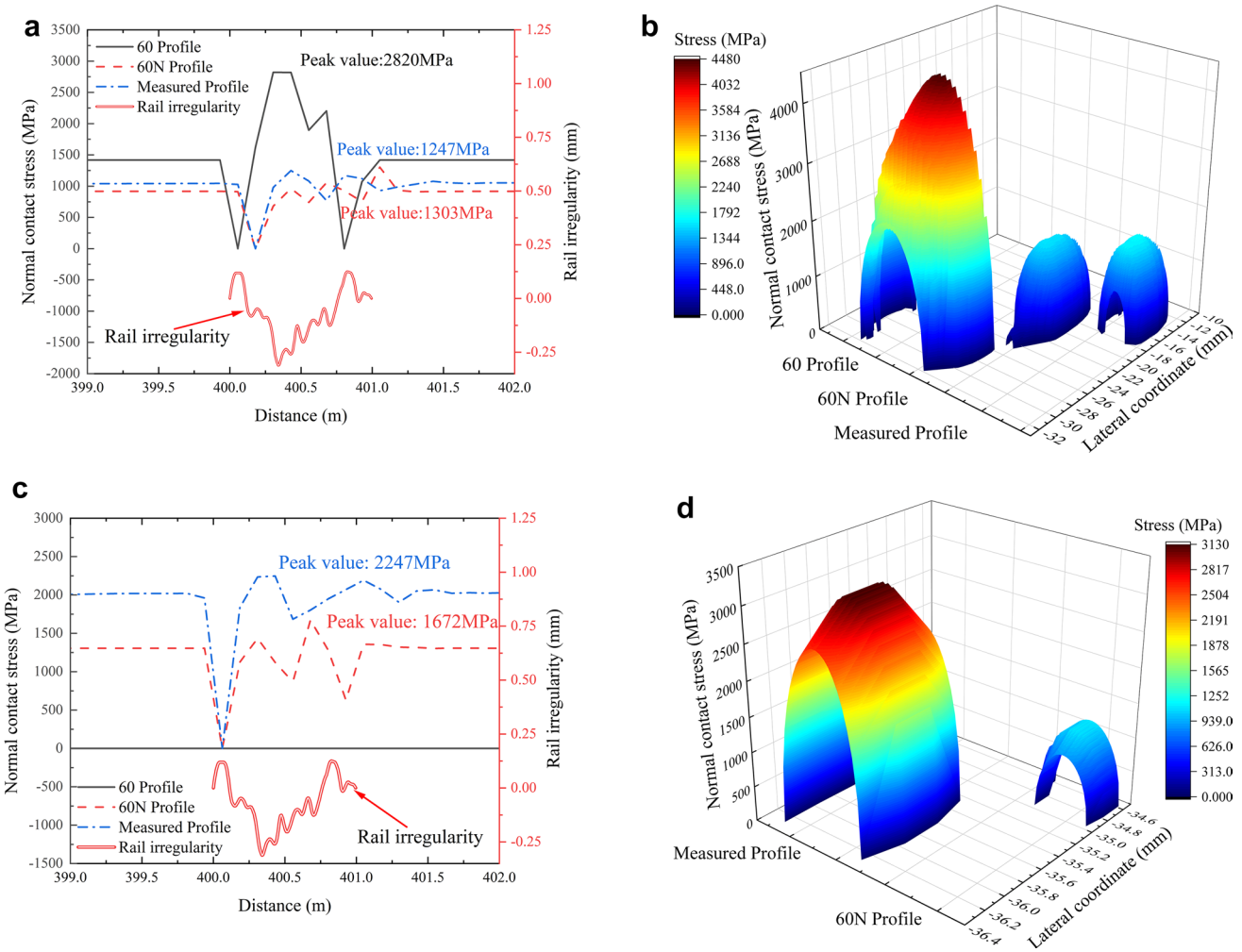

Fig. 12 Normal contact stress

and 1690 MPa, respectively, representing reductions of 64% and 62%.

Similar to Sect. 4.1, both the 60N profile and measured profile exhibit two-point contact phenomena. At the gauge corner, the normal stress peak for the measured profile is 2247 MPa, while the 60N profile shows 1672 MPa, a reduction of 26%. For maximum normal stress within contact patches, the measured profile shows 3130 MPa while the 60N profile shows 1112 MPa, a reduction of up to 64%.

Analysis results indicate that the 60 profile generates the highest contact stress under rail irregularity excitation, significantly accelerating plastic strain accumulation and fatigue defect deterioration. Although the measured profile and 60N profile show similar contact stresses at the rail running surface, the 60N profile exhibits significantly lower contact stress at the gauge corner.

Tangential stress comparative analysis (Fig. 13) shows that the 60N profile performs optimally across all indicators. In the running surface contact area, the maximum tangential stress for the 60 profile condition is 2114 MPa, the measured profile is 840 MPa, and the 60N profile is 832 MPa. The 60N profile shows reductions of 61% and 1%, respectively. In the gauge corner contact area, the maximum tangential stress for the measured profile is 1505 MPa, while the 60N profile shows 832 MPa, a reduction of 45%.

4.3 Including Track Excitation Condition

Changes in rail profiles not only affect wheel-rail contact stress distribution but also significantly impact wheel-rail fatigue, wear, and vehicle performance. To comprehensively evaluate the overall performance of the three profiles, wheel-rail surface fatigue index I , wear number W , and vehicle lateral vibration responses were calculated and analyzed using measured metro track irregularities as input excitation.

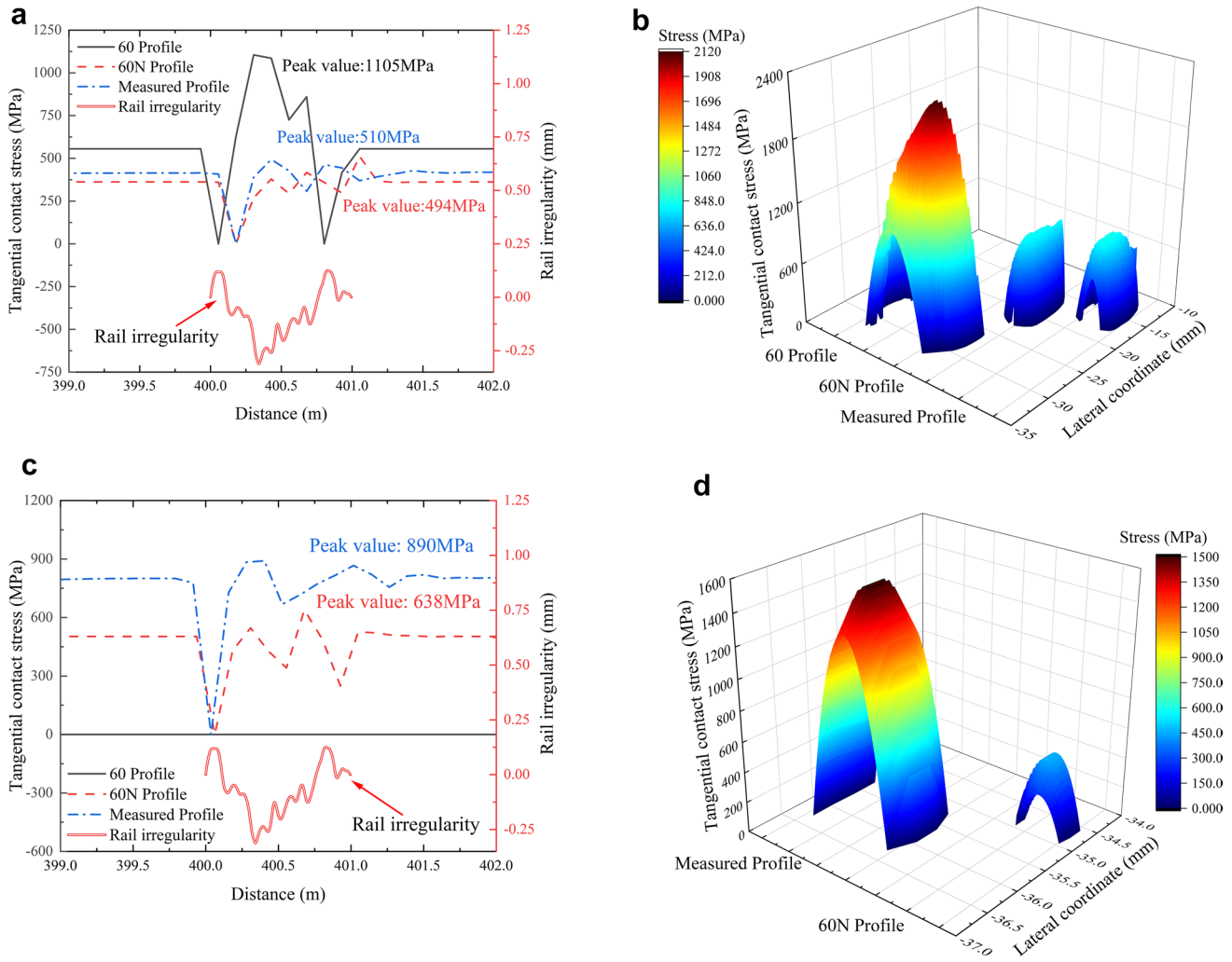

Fig. 13 Comparison of wheel-rail contact tangential stress

$$\begin{cases} I = \dfrac{\sqrt{T_x^2 + T_y^2}}{F_z} - \dfrac{Ak}{3F_z} \\ W = T_x\xi_x + T_y\xi_y \end{cases} \tag{8}$$

where, T_x represents the longitudinal creep force, T_y represents the lateral creep force, F_z represents the normal force, A represents the contact patch area, k represents the yield strength, ξ_x represents the longitudinal creepage, ξ_y represents the lateral creepage.

According to the reference [22], when the wheel-rail surface fatigue index exceeds 0, wheel-rail material deformation will experience ratcheting effects with continuous plastic deformation accumulation. A higher wear number indicates a faster wear rate. The calculation results are shown in Fig. 14.

Simulation results indicate that after the vehicle enters curve sections, both fatigue and wear indices increase rapidly. The fatigue indices for the 60 profile and measured profile stabilize around 0.25 and 0.2, respectively, while the 60N profile shows a fatigue index of approximately 0.1, indicating significantly slower plastic deformation accumulation.

Wear number comparison shows minimal differences between the 60N profile and measured profile when first entering curve sections. However, after a running distance of 500 m, the wear index under measured profile condition begins to increase sharply, exceeding baseline values by more than 5 times, while the 60N profile condition maintains stable. These results demonstrate that the 60N profile can effectively reduce wheel-rail fatigue development rates and wear rates.

Bogie and car body lateral acceleration comparison results are shown in Fig. 15. When using the 60N profile, bogie lateral acceleration consistently maintains the minimum value, with peak values reduced by 24% and 7% compared to the 60 profile and measured profile, respectively.

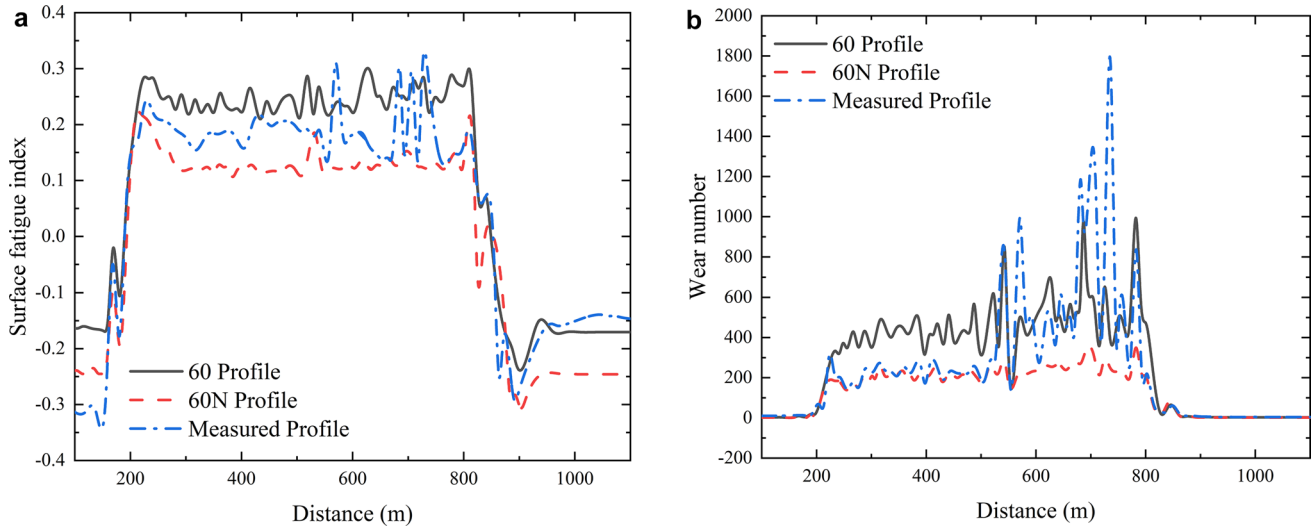

Fig. 14 Wheel-rail contact fatigue index and wear number

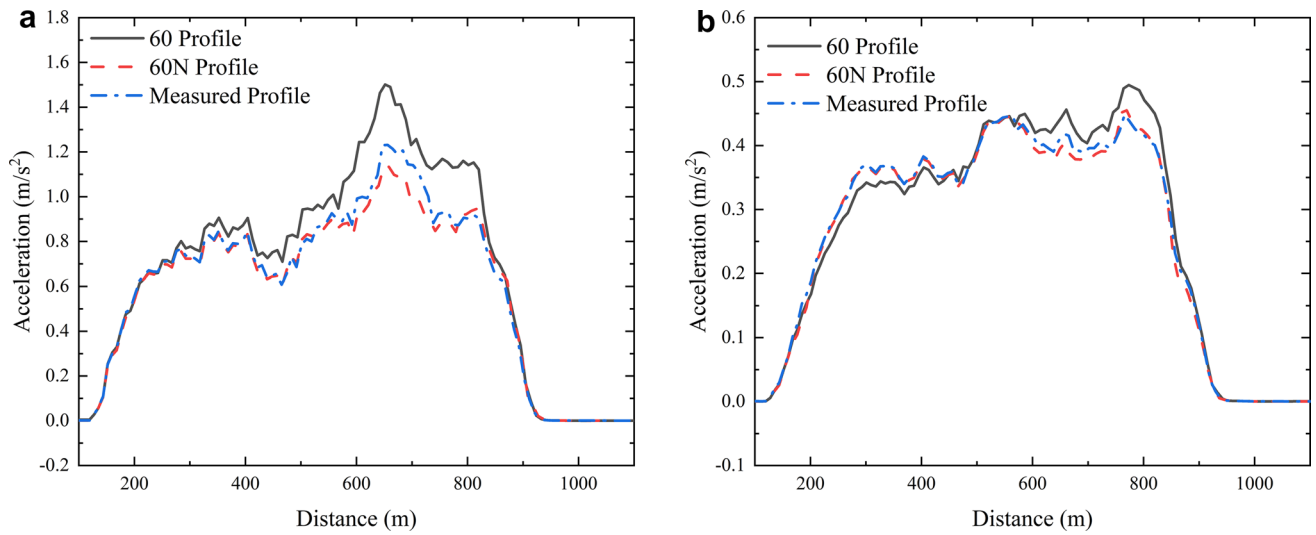

Fig. 15 Vehicle lateral acceleration

For car body acceleration, although the 60N profile condition is slightly higher than the 60 profile in the first 500 m section, the peaks occurring after 500 m are significantly lower than those of the 60 profile. Dynamic simulation results indicate that adopting the 60N profile can improve vehicle lateral stability to some extent.

Comprehensive analysis of wheel-rail contact stress, fatigue and wear indices, and vehicle dynamic responses under three operating conditions demonstrates that the 60N profile exhibits minimum normal and tangential stresses at the rail running surface. Additionally, it demonstrates the lowest fatigue index and wear number, effectively delaying wheel/rail material fatigue defect accumulation and wear development while exhibiting better vehicle lateral stability. Therefore, the 60N profile is more suitable for the operating conditions of this line.

5 Conclusion and Prospects

Addressing the severe rail fatigue defect problem in sharp radius curves of urban rail transit, this paper combines field investigation and testing with simulation analysis methods, taking Metro Line 2 in City N as the research object. A metro vehicle-track coupled dynamics model was established to systematically compare and analyze

the matching performance of the 60 profile, 60N profile, and measured profile, identifying the 60N profile as the optimal rail profile solution for this line.

(1) Field investigation revealed that severe rail scaling occurs on the high rail of sharp-radius curves, forming continuous multi-short-wave irregularities that intensify wheel-rail vibration and fatigue deterioration. The measured rail profiles exhibited negative deviations with small gauge corner curvature, and vehicles operated with approximately 60 mm excess superelevation, collectively contributing to fatigue defect development.
(2) A validated metro vehicle-track coupled dynamics model based on measured wheel profiles was established. Model reliability was validated through comparison with track inspection vehicle data and wayside dynamics test data, demonstrating high consistency in key parameters including car body acceleration, wheelset lateral forces, and derailment coefficients, confirming the model's effectiveness for wheel-rail matching analysis.
(3) Profile evaluation through comprehensive analysis of contact stress, fatigue, wear, and vehicle dynamics demonstrated that the 60N profile consistently exhibits superior performance. Compared to the 60 profile and measured profile, the 60N profile significantly reduces contact stresses and the values of fatigue index, maintains stable wear characteristics during operation, and improves vehicle lateral stability. Based on these findings, the 60N profile is recommended as both the original rail profile selection and grinding target profile for the metro line.

The methodology developed in this study—encompassing field investigation, validated modeling, and profile evaluation—provides a systematic framework that can be generalized to other metro systems. This integrated approach establishes a complete closed-loop from field problems to theoretical research and practical application. For other metro lines experiencing similar rail fatigue issues, the same methodology can be applied: (1) conducting field measurements of wheel-rail profiles, rail irregularities, and rail defect conditions; (2) establishing a validated vehicle-track coupled dynamics model based on measured data; (3) performing comparative analysis of different rail profile options to identify optimal solutions. Furthermore, the validated model developed in this study can also be directly adapted to other metro lines or sections with similar operating conditions by updating the measured profile and rail/track irregularity inputs. This transferable methodology provides a practical and efficient approach for rail profile selection and maintenance strategy optimization across various urban rail transit systems, contributing to more comprehensive support for full lifecycle management of metro rails.

Given the difficulty in controlling rail profile grinding quality in curve sections, future work will continue to investigate and monitor the rail grinding profile quality of this line, comprehensively considering the impact of profile deviations caused by grinding operations, and researching and optimizing rail grinding schemes; Furthermore, after rail grinding or major replacement, continuous tracking and observation of rail surface service conditions and profile evolution characteristics will be conducted to deeply analyze wheel-rail interaction mechanisms at different service stages and develop scientific and effective maintenance strategies, providing more comprehensive theoretical support and practical guidance for full lifecycle management of urban rail transit rails.

Acknowledgments The authors are grateful to the journal editor and reviewers.

Author contributions Bolun An contributed to writing original draft, software, data curation, methodology, formal analysis. Wei Lu contributed to investigation, data curation. Fengshou Liu and Hao Liu worked in supervision, resources and funding acquisition. Yang Xu contributed to conceptualization. Sen Wang contributed to the validation.

Funding This work was supported by the National Key Research and Development Program of China (Grant No. 2021YFB2601000), the Technology Research and Development Plan of China Railway (Grant No. K2024G009), the Fund of China Academy of Railway Sciences Corporation Limited (Grant No. 2024YJ200).

Data Availability The data underlying this article will be shared on reasonable request to the first author.

Declarations

Conflict of interest The authors declare that they have no conflict of interest.

References

1. Wang S, Wen B, Ren D, Ding Y, Wen Z, Dong D, Tao G (2024) Analysis of the causes of severe side wear of the high rail on metro curves by numerical simulation and field investigation. P I MECH ENG F-J RAI 238(4):381–393. https://doi.org/10.1177/09544097231193274
2. Li C, Guan Q, Xu S, Wen Z, Tao G (2023) Analysis on formation mechanism of double contact bands on metro rails. J Cent South Univ Sci Technol 54(4):1633–1643
3. Guan Q, Li C, Xu S, Wen Z, Lu W, Jin X (2023) Formation mechanism of the double contact bands on the wheel and rail treads of a metro system. Wear. https://doi.org/10.1016/j.wear.2023.205122
4. Cui X, Tang C, Lv D, Li T, Xu J, Zhong J (2023) Grinding limit and profile optimization in the high-incidence section of rail corrugation in mountainous city metro. Wear. https://doi.org/10.1016/j.wear.2023.204850
5. Ren D, Tao G, Li W, Lu W, Wen Z, Jin X (2022) Investigation on abnormal wear of metro wheels through simulations of wheel/rail profile matching. J Mech Eng 58(10):191–199
6. Qi Y, Dai H, Song Y, Ye Y, Li D (2024) Optimisation design of grinding rail profile of metro lines for small radius curved track based on the GFC method: a case study. Veh Syst Dyn 62(8):1929–1951. https://doi.org/10.1080/00423114.2023.2270590
7. Shi J, Gao Y, Long X, Wang Y (2021) Optimizing rail profiles to improve metro vehicle-rail dynamic performance considering worn wheel profiles and curved tracks. STRUCT MULTIDISCIP O 63(1):419–438. https://doi.org/10.1007/s00158-020-02680-7
8. Cuervo PA, Santa JF, Toro A (2015) Correlations between wear mechanisms and rail grinding operations in a commercial railroad. Tribol Int 82:265–273. https://doi.org/10.1016/j.triboint.2014.06.025
9. Tao G, Wen Z, Lu W, Jin X (2015) Static contact analysis of matching relationship of metro vehicle wheel and rail profiles under different rail cant conditions. J China Railway Soc 37(9):82–89
10. Zhou S, Xue R, Zhang Q, Zheng X (2016) Wheel-rail rolling contact finite element analysis of the wear state on the curve of subway line. J Mech Eng 52(12):129–135. https://doi.org/10.3901/jme.2016.12.129
11. Tao G, Wen Z, Lu W, Jin X (2016) Dynamic analysis of wheel and rail profile matching relationship for metro vehicle under different rail cant conditions. J China Railway Soc 38(5):16–22
12. Chen R, Wen J, Yu H, An B, Xu J, Wang P (2020) Influence of rail gauge on wheel-rail contact behavior of metro line. J Cent South Univ Sci Technol 51(3):824–831
13. Yang F, Gao L (2025) Multi-objective optimization of the asymmetric-grinding rail profile for sharply curved tracks on metro line. Int J Non-Linear Mech. https://doi.org/10.1016/j.ijnonlinmec.2025.105065
14. Cui D, Fu Y, Wu Y, Lu P, Liu T, Zhang X (2024) Optimisation of rail profile and grinding pattern in the curve section of a subway. Veh Syst Dyn 62(7):1827–1847. https://doi.org/10.1080/00423114.2023.2266531
15. An B, Yang G, Liu J, Liu F, Shi T, Du J (2025) Optimising the rail profile for reducing wheel-rail creepage and contact stress in high-speed railway curves. Veh Syst Dyn. https://doi.org/10.1080/00423114.2025.2544341
16. Zhou Q, Zhang Y, Tian C, Chen Z, Liu F, Yu Z, Li L (2014) Profile design and test study of 60NRail. China Railway Sci 35(2):128–135
17. Wang P, An B, Ma J, Wang S, Liu F (2024) Theoretical and experimental research on the influence and optimization method of the 60N profile in turnout. Int J Struct Stab Dyn. https://doi.org/10.1142/S0219455424501475
18. Liu G, Chen S, Liu S, Jin H, Wang D (2021) Maintenance arrangement optimization for infrastructure systems of urban rail transit considering resource constraints. J Transpo Syst Eng Inf Technol 21(3):163–169
19. An B, Wang P, Ma S, Ma Z, Zhong Y, Zhao W (2022) Influence of metro track irregularities on pantograph vibration and its interaction with catenary. Appl Sci. https://doi.org/10.3390/app12136435
20. Piotrowski J, Kik W (2008) A simplified model of wheel/rail contact mechanics for non-Hertzian problems and its application in rail vehicle dynamic simulations. Vehicle Syst Dyn 46(1–2):27–48. https://doi.org/10.1080/00423110701586444
21. Ayasse JB, Chollet H (2005) Determination of the wheel rail contact patch in semi-Hertzian conditions. Vehicle Syst Dyn 43(3):161–172. https://doi.org/10.1080/00423110412331327193
22. Ekberg A, Kabo E, Andersson H (2002) An engineering model for prediction of rolling contact fatigue of railway wheels. Fatigue Fract Eng Mater Struct 25(10):899–909. https://doi.org/10.1046/j.1460-2695.2002.00535.x